PCCP

Deep-red to near-infrared luminescence from Eu^{2+}-trapped exciton states in YSiO$_2$N

SCHOLARONE™
Manuscripts

Deep-red to near-infrared luminescence from Eu^{2+}-trapped exciton states in $YSiO_2N$

Yuuki Kitagawa,[a]* Jumpei Ueda,[a] Jian Xu,[b] Takayuki Nakanishi,[c] Takashi Takeda,[c] Naoto Hirosaki,[c] Setsuhisa Tanabe[a]

[a] Department of Interdisciplinary Environment, Graduate School of Human and Environmental Studies, Kyoto University, Kyoto 606-8501, Japan

[b] International Center for Young Scientists (ICYS), National Institute for Materials Science (NIMS), Tsukuba, Ibaraki 305-0044, Japan

[c] Luminescent Materials Group, National Institute for Materials Science (NIMS), Tsukuba, Ibaraki 305-0044, Japan

*Corresponding author: Y. Kitagawa; kitagawa.yuuki.66w@st.kyoto-u.ac.jp

† Electronic supplementary information (ESI) available.

Abstract

The valence state of Eu ions doped in inorganic compounds is easily influenced by the synthesizing condition. In this study, the X-ray absorption spectroscopy revealed that almost half of Eu ions incorporated in the $YSiO_2N$ host were reduced into the divalent state through the sintering process at 1600 ºC under the N_2 gas atmosphere without any annealing processes. The prepared $Eu^{2+/3+}$-doped $YSiO_2N$ sample showed the anomalous deep-red to near-infrared luminescence below 300 K under violet light illumination, whose luminescent properties are discussed with the detailed spectroscopic analyses. In the photoluminescence spectra at 4 K, the broad luminescence band ranging from 550 to 1100 nm with a large Stokes shift of 5677 cm^{-1} was observed, assigned to the recombination emission related to the Eu^{2+}-trapped exciton state. The temperature dependence of luminescence lifetime suggests that the thermal quenching of Eu^{2+}-trapped exciton luminescence takes place through complicated processes in addition to thermal ionization. The energy diagrams based on the spectroscopic results indicate that Eu^{2+}-trapped exciton luminescence in the $YSiO_2N$:$Eu^{2+/3+}$ sample was observed because all the Eu^{2+}: 5d excited levels are degenerated with the host conduction band, and the relatively stable Eu^{2+}-trapped exciton state in the Y^{3+} sites is formed just below the conduction band bottom. The comprehensive discussion on the deep-red to near-infrared luminescence in the $YSiO_2N$ host could give new insights into the mechanism of Eu^{2+}-trapped exciton luminescence in Y^{3+} sites, which has the potential to the near-infrared emitting devices.

1   Introduction

Divalent europium ion (Eu^{2+}) is one of the most studied luminescence centers for functional luminescent materials activated with lanthanoid ions. Its applications are various; *e.g.,* solid-state lighting,[1–3] high-resolution LED displays,[4,5] and persistent phosphors.[6,7] Eu^{2+} ions in inorganic compounds show highly efficient luminescence due to the parity allowed 5d $\rightarrow$ 4f transition. Unlike the Ce^{3+}: 5d $\rightarrow$ 4f luminescence, the typical luminescence lifetime of Eu^{2+} is relatively long, 0.4–3.3 µs,[8,9] due to the partially spin-forbidden transition from the mixing state of sextet and octet $4f^6 5d^1$ to $4f^7$ $^8S_{7/2}$ levels. The luminescence wavelengths are correlated with the anion species coordinating around Eu^{2+} ions and crystal field.[10,11] In terms of tailoring the luminescence color, the 5d energy shift in a specific ligand field has been studied in a variety of compounds. Recently, more and more researchers have been focusing on the exploration of materials showing the broadband deep-red and near-infrared (NIR) luminescence for applications, such as lighting, sensing, and bio-imaging devices.[12–14] The deep-red to NIR phosphors in many reports utilize the Cr^{3+}: 3d-3d luminescence in the octahedral coordination.[15] On the other hand, there are not so many examples of deep-red to NIR luminescence of Eu^{2+}-doped oxides despite the broadband luminescence through highly efficient 5d-4f parity allowed transition.[16–21] For materials exploration, (oxy)nitrides can be a desirable host compound for the deep-red to NIR phosphors because of the redshifted Eu^{2+} luminescence caused by the large nephelauxetic effect of nitrogen.[22] In literature, there are only a few reports about the deep-red to NIR emitting Eu^{2+}-doped nitrides with a luminescence peak λ_{em} over 700 nm, such as $Mg_3(BN_2)N:Eu^{2+}$ (λ_{em} = 710 nm)[23] and $Ca_3Mg[Li_2Si_2N_6]:Eu^{2+}$ (λ_{em} = 734 nm).[24]

However, luminescence in the Eu^{2+}-doped compounds is not always attributed to the Eu^{2+}: 5d $\rightarrow$ 4f transition. For example, the $BaS:Eu^{2+}$ shows NIR luminescence peaking at 878 nm at

ambient temperature with quite broad widths of 3980 cm^{-1}.[25] This luminescence is not anticipated from the chemical trend of Eu^{2+}: 5d → 4f transition in *AE*S materials (*AE* = Ca, Sr, and Ba). Such anomalous luminescence is attributed to the recombination emission from the impurity-trapped exciton state.[26,27] The features and problems of anomalous luminescence related to Eu^{2+}- or Yb^{2+}-trapped exciton states have been reviewed in Dorenbos's report.[26] The impurity-trapped exciton state takes large lattice relaxation, resulting in the anomalously broad and redshifted luminescence band with a large Stokes shift. Recently, some studies have claimed that the mechanism of anomalous luminescence is due to the intervalence charge transfer (IVCT) transition.[28,29]

In this study, the Eu^{2+}-related luminescence in the YSiO$_2$N host is characterized and discussed. Previously, we have reported the intense red luminescence of the Eu^{3+}-doped YSiO$_2$N phosphor under near-UV excitation.[30,31] While the as-made YSiO$_2$N:Eu^{3+} sample, which was prepared by the solid-state reaction at 1600 °C under N$_2$ gas flow, showed the strong absorption band in the range of 380–500 nm and weak Eu^{3+} luminescence, the annealing process of the sample at 700 °C under N$_2$ gas flow successfully enhanced Eu^{3+} luminescence intensity.[30] According to the Ellingham diagram,[32] this enhancement was possibly due to the oxidization of Eu ions that were reduced into the divalent state during the high-temperature synthesis under the inert atmosphere. However, there was no direct evidence showing the existence of Eu^{2+} ions. First, we reveal the valence state of Eu ions in the as-made and annealed YSiO$_2$N:Eu sample with the X-ray absorption spectroscopy, and discuss the suitable sintering condition for Eu^{2+}- or Eu^{3+}-doped oxynitride phosphors. Besides, we find that the Eu$^{2+/3+}$-doped YSiO$_2$N sample shows the deep-red to NIR luminescence ranging from 550 to 1100 nm at low temperatures below 300 K and investigate the properties of this anomalous luminescence for the assignment; whether the Eu^{2+}: 5d → 4f transition or the recombination emission related to the impurity-trapped exciton states.

2   Experimental procedure

2.1   Sample Preparation

Polycrystalline ceramic $YSiO_2N$ samples doped with 1.0% Eu ions, $Y_{0.99}Eu_{0.01}SiO_2N$, were prepared by the solid-state reaction method. The starting chemicals Y_2O_3 (99.99%, Kojundo Chemical Laboratory), SiO_2 (99.9%, Kojundo Chemical Laboratory), Si_3N_4 (99.9%, Kojundo Chemical Laboratory), and Eu_2O_3 (99.99%, Furuuchi Chemical) were weighed in the glove box filled with high-purity Ar gas. Powders of chemicals were mixed with a ball milling system (Premium Line P-7, Fritsch) with ethanol (>99.5%). The obtained slurry was dried at 120 °C for 24 h. The mixture was pelletized with dry pressing and put in an inner alumina crucible. This crucible was set in another large alumina crucible with carbon powder, and then sintered at 1600 °C under N_2 gas flow for 24 h. One of the as-made samples was annealed at 700 °C under N_2 gas flow for 24 h. The crystalline phase of the prepared samples was confirmed by X-ray diffraction (XRD) measurements with a diffractometer (Rigaku, Ultima IV). The XRD patterns are given in Fig. S1 (ESI†). As a reference, the simulated diffraction pattern of the monoclinic $YSiO_2N$ was simulated with the VESTA program.[31,33]

2.2   Characterization

The X-ray absorption spectroscopy (XAS) was performed at the beamline BL-9A of Photon Factory (KEK, Japan). The Eu L_{III} X-ray absorption near edge structure (XANES) spectra were recorded in the transmission mode. As references, $EuCl_2$ and EuN chemicals were also measured. Obtained data were analyzed with the Athena software package.[34]

Photoluminescence excitation (PLE) spectra at 4 K were measured by monochromatic excitation light with a 500 W Xe short arc lamp (OPM2-502XQ, Ushio Inc.) equipped with a

double monochromator system by two monochromators (SP-300i, Acton Research Corp.), detected by using a photomultiplier tube (PMT) detector (R10699, Hamamatsu Photonics) coupled with a monochromator (SP-2300i, Princeton Instruments). The obtained PLE spectra were calibrated by the spectrum of the Xe lamp (light source) detected by a calibrated Si photodiode (S1337-1010BQ, Bunkoukeiki Co., Ltd.). For photoluminescence (PL) measurements, the sample was excited by the monochromatic excitation light of the Xe lamp or a 405 nm laser diode (LD) (SDL-405-LM-100T, Shanghai Dream Lasers Technology), and luminescence was detected with a Si CCD spectrometer (λ < 1050 nm, QE65Pro, Ocean Optics) and an InGaAs spectrometer (950 < λ < 1650 nm, NIRQuest-512-1.7, Ocean Optics) connected with UV-VIS or NIR optical fibers. The obtained PL spectra were calibrated by the spectrum of a deuterium-tungsten halogen light source (DH-2000, Ocean Optics). The sample temperatures were controlled by a cryostat with a closed-cycle He gas cryogenic refrigerator (CRT-A020-SE00, Ulvac Cryogenics). The diffuse reflectance spectra at the ambient temperature were collected by a UV-VIS-NIR spectrophotometer (UV-3600, Shimadzu) equipped with an integrating sphere.

Time-resolved luminescence spectroscopy of the bulk sample was performed on an optical setup mainly consisting of Ti:Sapphire solid-state laser with optical parametric generator (OPG), 3D Raman confocal microscope system, high-resolution monochromator, and streak camera. The sample was excited with OPG (Chameleon Vision-S, Coherent, inc.) pumped by a pulsed Ti:Sapphire laser with emission wavelength at 800 nm, which was able to generate the SHG laser beam at 400 nm with 75 fs pulse width and 50 MHz repetition rate. The 3D Raman confocal microscope system (Nanofinder 30, Tokyo Instruments, Inc.) acts as a real-time imaging spectrometer to monitor the emission from the phosphor under the OPO laser excitation. The reflected optical signal through a fluorescence microscope (BX51M, Olympus Co., Ltd.) was

collected by a high-resolution monochromator (SpectraPro HRS-300, Princeton Instruments) and a streak camera (C14831-110, Hamamatsu Photonics). The emission spectral range was monitored between 430 nm and 800 nm with a 40 g/mm grating groove. Timescales for measurement were set to be 500 ns/20 ns, and temperature dependence experiments were performed in a microscopy cryostat (Janis ST-500, Lake Shore Cryotronics) with temperature control at 4, 150, and 300 K.

The luminescence decay measurements at low temperatures ($T = 20$–300 K) were measured by a luminescence lifetime spectrometer (Quantaurus-Tau, Hamamatsu Photonics), using a time-correlated single-photon counting (TCSPC) method under excitation with a 405 nm pico-second LED. The sample temperature was controlled by a closed-cycle He cryostat (Mini Stat CRT-006-2600, Iwatani).

3   Results and discussion

3.1   Determination of valence states of europium ions in $YSiO_2N$
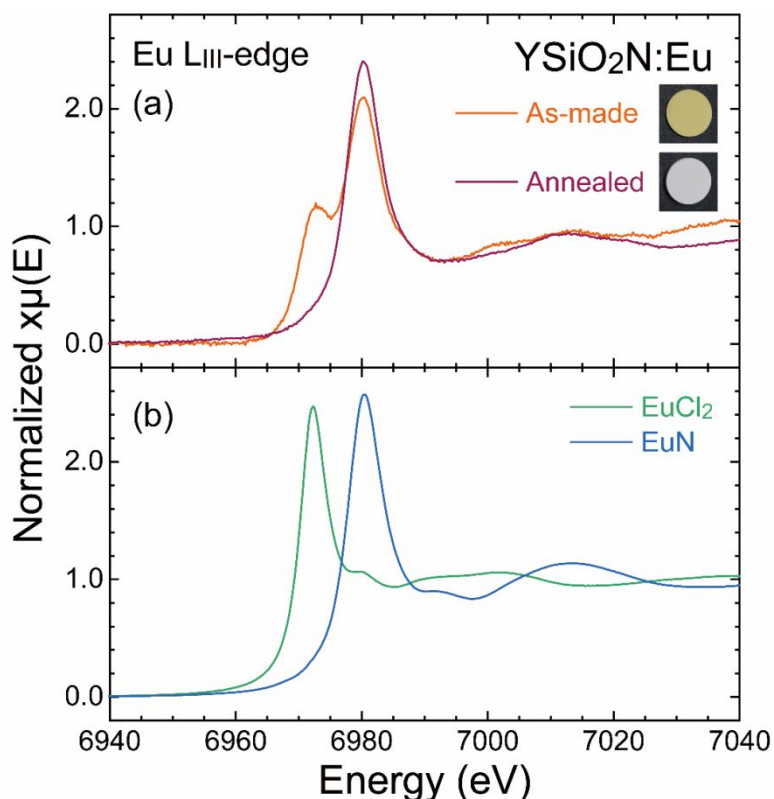
Fig. 1 Normalized Eu L_{III}-edge XANES spectra of (a) as-made and annealed Eu-doped $YSiO_2N$ samples, and (b) $EuCl_2$ and EuN chemicals as references for divalent and trivalent states. The photographs of the as-made and annealed samples are given in the inset.

We investigated the valence state of Eu ions in the as-made (body color: yellow) and annealed (body color: white) samples to discuss the effect of the annealing process for the Eu-doped $YSiO_2N$. Fig. 1a shows the normalized Eu L_{III}-edge XANES spectra for the as-made and annealed $YSiO_2N$:Eu samples. The XANES spectra of the reference chemicals for divalent and trivalent Eu

ions, Eu(II)Cl$_2$ and Eu(III)N, are displayed in Fig. 1b. The annealed sample shows a white line at 6980 eV, corresponding to the X-ray absorption peak of Eu^{3+}. In the annealed YSiO$_2$N:Eu sample, all the Eu ions take the trivalent state. Therefore, the annealing process at 700 ºC under the N$_2$ atmosphere is very effective in obtaining intense Eu^{3+} luminescence in oxynitride hosts. On the other hand, the as-made sample shows another peak at 6974 eV, which is in accordance with the X-ray absorption peak of Eu^{2+}, in addition to the Eu^{3+} peak at 6980 eV. The existence of Eu^{2+} indicates that some Eu^{3+} ions doped as Eu$_2$O$_3$ were reduced into divalent states in the YSiO$_2$N host with high-temperature synthesis at 1600 °C under an inert atmosphere. By performing the linear combination fitting of the Eu^{2+} and Eu^{3+} peaks,[35] the amount of Eu^{2+} ions is estimated to be 46.5% (Fig. S2, ESI†). Almost half of Eu ions were reduced into divalent states, leading to the as-made sample composition of Y$_{0.99}$Eu$^{2+}_{\sim 0.005}$Eu$^{3+}_{\sim 0.005}$SiO$_2$N, after this called YSiO$_2$N:Eu$^{2+/3+}$.

3.2 Characterization of anomalous deep-red to NIR luminescence in YSiO$_2$N:Eu$^{2+/3+}$
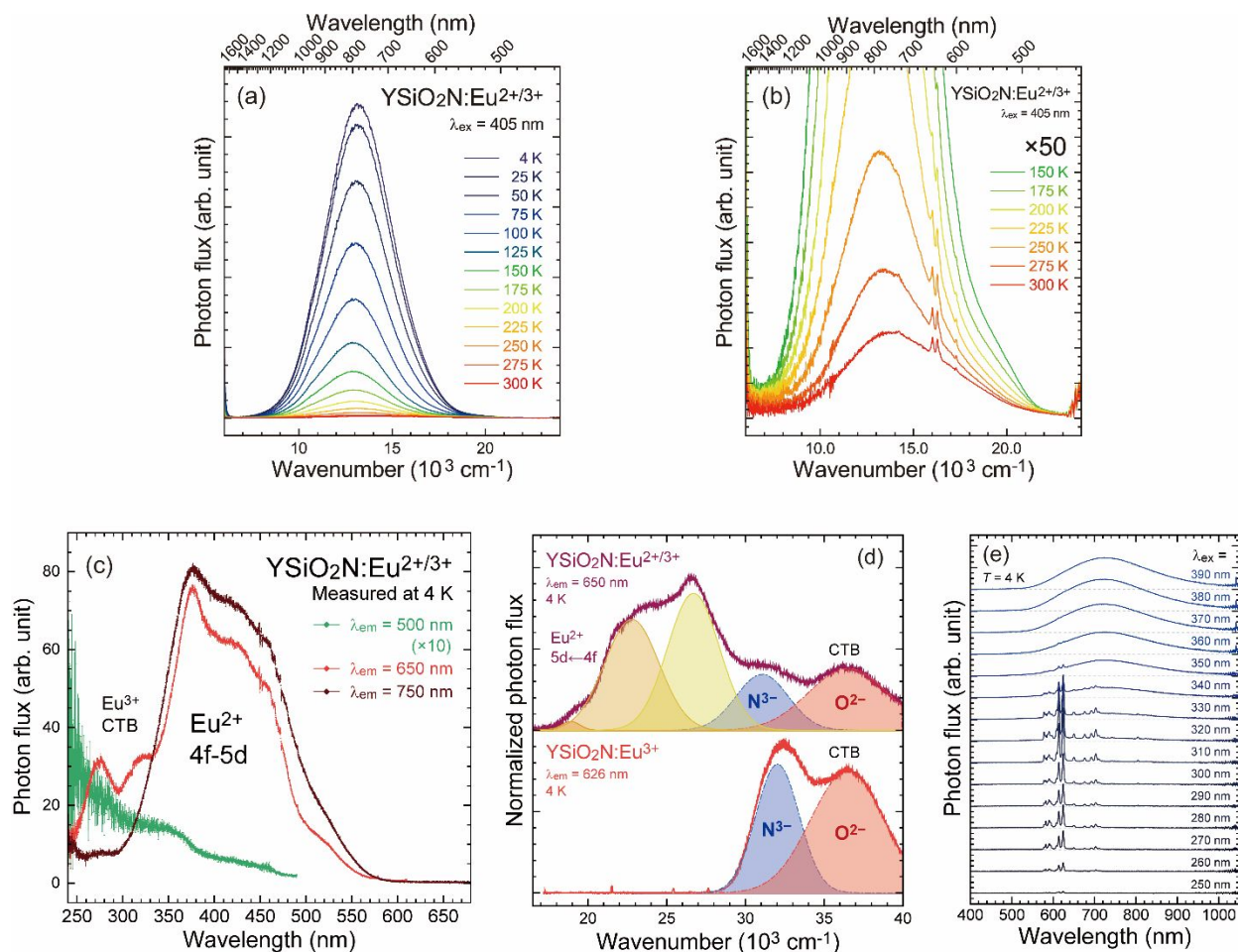
Fig. 2 (a) PL spectra of the YSiO$_2$N:Eu$^{2+/3+}$ sample at low temperatures (T = 4–300 K), excited with a violet LD (λ_{ex} = 405 nm). (b) Enlarged PL spectra shown in Fig. 2a (×50). (c) PLE spectra at 4 K with different monitored wavelengths (λ_{em} = 470–750 nm). (d) Normalized PLE spectra for the as-made YSiO$_2$N:Eu$^{2+/3+}$ and annealed YSiO$_2$N:Eu^{3+} samples at 4 K. The Gaussian profiles after deconvolution are shown in overshadowed. (e) PL spectra at 4 K with different excitation wavelengths (λ_{ex} = 250–390 nm).

Because the yellow as-made $YSiO_2N:Eu^{2+/3+}$ sample shows very weak luminescence at room temperature under UV excitation, the sample was cooled down to 4 K, resulting in the strong deep-red to NIR luminescence with a violet LD excitation ($\lambda_{ex} = 405$ nm). Fig. 2a shows the PL spectra of the $YSiO_2N:Eu^{2+/3+}$ sample at various temperatures ($T = 4$–300 K). At 4 K, the $YSiO_2N:Eu^{2+/3+}$ sample shows a strong and broad luminescence band peaking at 13229 cm^{-1} (= 756 nm) by the 405 nm excitation. The full width at half maximum (FWHM) of this band is 4061 cm^{-1}, which is broader even at 4 K than the typical bandwidth for Eu^{2+}-doped compounds, 800–3500 cm^{-1}.[10,26] Compared with many Eu^{2+}-activated (oxy)nitride phosphors,[22] such as α-Ca-SiAlON:Eu^{2+} ($\lambda_{em} = 585$ nm),[36–40] $CaAlSiN_3:Eu^{2+}$ ($\lambda_{em} = 650$ nm),[1] and $Sr[LiAl_3N_4]:Eu^{2+}$ ($\lambda_{em} = 650$ nm),[4] the $YSiO_2N:Eu^{2+/3+}$ sample shows the significant redshifted luminescence, unexpected from the host chemical composition of $YSiO_2N$. These spectroscopic features suggest that anomalous deep-red to NIR luminescence is not attributed to Eu^{2+}: 5d → 4f transition.

The PL intensity of the $YSiO_2N:Eu^{2+/3+}$ sample decreases monotonously over 4 K. At 200 K, the PL intensity is less than only 10% of the initial PL intensity at 4 K. Over 200 K, the additional luminescence components appear as the anomalous deep-red to NIR luminescence band is quenched with temperature. Fig. 2b shows the PL spectra enlarged by a factor of 50 ($T = 200$–300 K). Here, sharp luminescence bands assigned to the Eu^{3+} 4f-4f transition are observed in the range of 15500–17500 cm^{-1}. In addition, the bandwidth of the broad luminescence gets larger, probably due to the additional band in the range of 15000–20000 cm^{-1} with a different thermal quenching behavior. In short, the PL spectra of the $YSiO_2N:Eu^{2+/3+}$ sample below ambient temperature ($T = 4$–300 K) indicate that there are at least three luminescence components with violet light excitation; (i) strong anomalous deep-red to NIR luminescence, (ii) considerably weak

visible luminescence, and (iii) Eu^{3+} luminescence at the Y sites. The thermal quenching behavior is discussed in detail in the following section.

Fig. 2c shows the PLE spectra at 4 K with different monitored wavelengths (λ_{em} = 500, 650, and 750 nm) to understand the excitation process for each luminescence component. In the PLE spectra (λ_{em} = 500 nm) of weak visible luminescence, an excitation plateau is observed in the range between 300 and 450 nm. In the PLE spectra of the deep-red to NIR luminescence (λ_{em} = 650, 750 nm), several excitation bands are observed below 600 nm. The strong excitation band in the range of 300–600 nm, especially in the PLE spectrum with λ_{em} = 750 nm, is assigned to the Eu^{2+}: 5d ← 4f transition because the spectral shape and range are similar to those of the Eu^{2+}: 5d ← 4f transition in oxynitrides, such as Ca-α-SiAlON and β-SiAlON.[22,37,39,41] This excitation band corresponds to the absorption band observed in the diffuse reflectance spectra (Fig. S3, ESI†). Here, no other absorption was observed over 650 nm, suggesting that the Eu^{2+}: 5d ← 4f transition is the dominant excitation pathway for the anomalous deep-red to NIR luminescence. In the diffuse reflectance spectra for the annealed $YSiO_2N$:Eu^{3+} sample, any absorption band was not detected in the visible range over 400 nm because the absorption coefficient of Eu^{3+}: 4f-4f forbidden transition is quite low. In the PLE spectra with λ_{em} = 650 nm, two additional excitation bands peaking at 276 and 315 nm are assigned to the charge transfer (CT) transition from coordinating anions (O^{2-} and N^{3-}) to Eu^{3+} because the Eu^{3+}: $^5D_0$ → $^7F_3$ luminescence is detectable simultaneously.[31] Considering these CT excitation bands, the PLE spectra with λ_{em} = 650 nm can be deconvoluted into five Gaussian profiles, two CT and three Eu^{2+}: 5d ← 4f bands. Fig. 2d shows the PLE spectra of the $YSiO_2N$:$Eu^{2+/3+}$ (as-made) and $YSiO_2N$:Eu^{3+} (annealed) sample with the results of Gaussian fitting. In the monoclinic $YSiO_2N$ host, there are five crystallographically nonequivalent [YO_6N_2] dodecahedral sites; one C_i site (Wyckoff 4*a*), one C_1 site (Wyckoff 8*f*),

and three C_2 sites (Wyckoff 4e).[31] The 5d excited levels of Eu^{2+} ions incorporated in these sites can be split into five due to the lower site symmetry. Besides, the Eu^{2+} $4f^65d^1$ electronic configuration brings about a more complicated energy level structure than the Ce^{3+} $4f^05d^1$ electronic configuration because of the spin polarization. Therefore, the Eu^{2+}: 5d ← 4f excitation band shows the complicated spectral shape with multiple Gaussian-shaped components, and it is difficult to reveal the precise number of the Gaussian functions to use. However, the purpose of the Gaussian deconvolution is not to calculate the precise 5d energies and energy level distributions but to estimate the energy of the lowest 5d excited level. In order to reproduce the PLE spectra band with the minimum numbers of the Gaussian functions, the Eu^{2+}: 5d ← 4f excitation band was fitted with just three Gaussian functions for simplicity. For the $YSiO_2N:Eu^{3+}$ sample, the excitation bands were deconvoluted into only two profiles of the CT transition from N^{3-} and O^{2-} to Eu^{3+} ions. Similarly, the Eu^{3+} CT bands for the $YSiO_2N:Eu^{2+/3+}$ sample were represented by two Gaussian functions with slightly broad widths because of the overlap with Eu^{2+} 5d bands. According to the Gaussian fitting, the lowest 5d band for Eu^{2+} is located at 18906 cm^{-1} (= 2.34 eV), which provides a large Stokes shift of 5677 cm^{-1} between the peaks of the luminescence band and the lowest 5d excitation band. Considering the typical Stokes shift for Eu^{2+}-activated phosphors of 800–4000 cm^{-1},[26,42,43] the Stokes shift of deep-red to NIR luminescence band for the $YSiO_2N:Eu^{2+/3+}$ sample is anomalous. According to Dorenbos, the anomalous luminescence of impurity-trapped exciton states in Eu^{2+}-doped materials has the following three features; (1) an abnormally large Stokes shift (5000–10000 cm^{-1}) and width (> 4000 cm^{-1} at ambient temperature) of the emission band, (2) an emission wavelength that is not consistent with the wavelength anticipated from the compositional and structural properties of compounds, and (3) an anomalous decay and thermal quenching behavior.[10,26] Therefore, The large

FWHM (4061 cm^{-1}) and the large Stokes shift (5677 cm^{-1}) for the YSiO$_2$N:Eu$^{2+/3+}$ sample suggest that the deep-red to NIR luminescence observed only in the as-made YSiO$_2$N:Eu$^{2+/3+}$ sample is related to the Eu^{2+}-trapped exciton (ETE) state.[26]

Fig. 2e shows the PL spectra at 4 K with various excitation wavelengths ($\lambda_{ex} = 250$–390 nm). Under the excitation light below 360 nm, sharp luminescence bands assigned to the Eu^{3+}: 4f-4f transition are observed. On the other hand, the deep-red to NIR ETE luminescence is observed with the excitation over 310 nm. These results are consistent with the deconvolution results of the PLE spectra shown in Fig. 2d, implying that ETE states and Eu^{3+} ions are excited only through the Eu^{2+}: 5d $\leftarrow$ 4f and CT transitions, respectively.
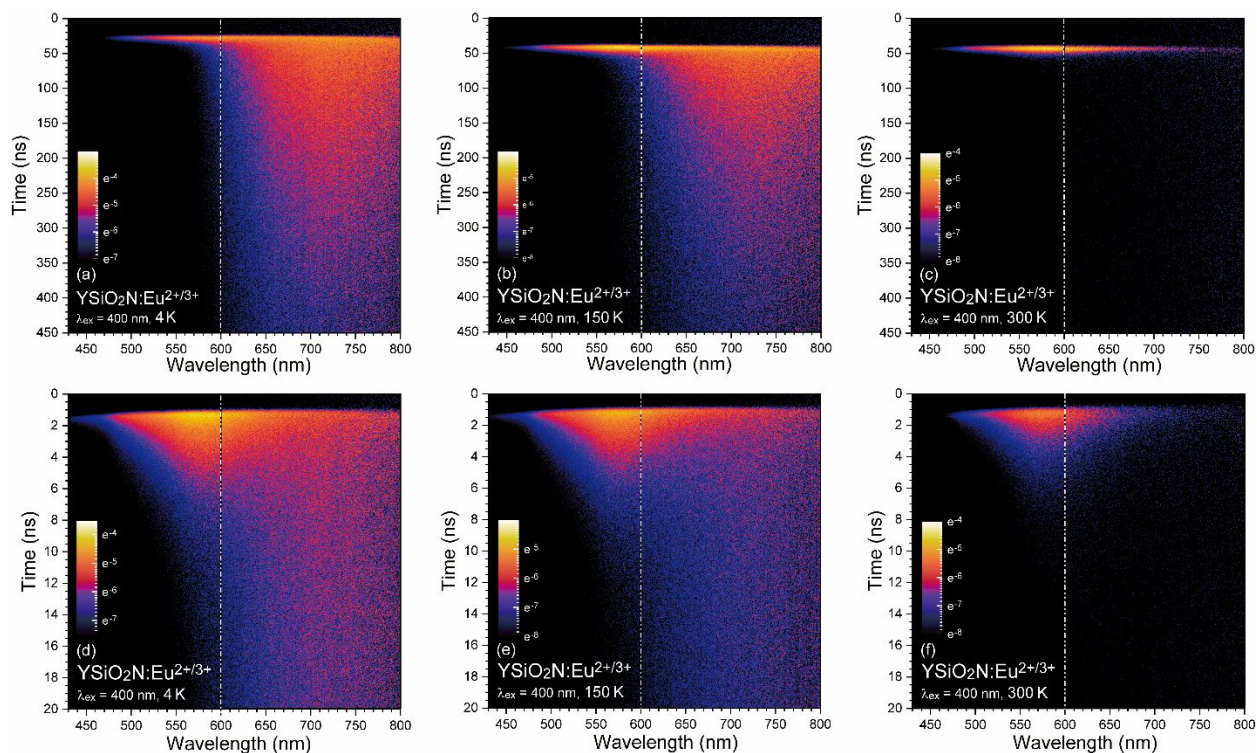
Fig. 3 Time-resolved PL spectra of the YSiO$_2$N:Eu$^{2+/3+}$ sample with different time ranges (0–450 and 0–20 ns) at different temperatures (T = 4, 150, 300 K). The PL intensities depending on monitored wavelengths were calibrated by the spectra with the continuous wave (cw) light source. Two spectra with the same condition were combined at 600 nm (shown with broken white lines).
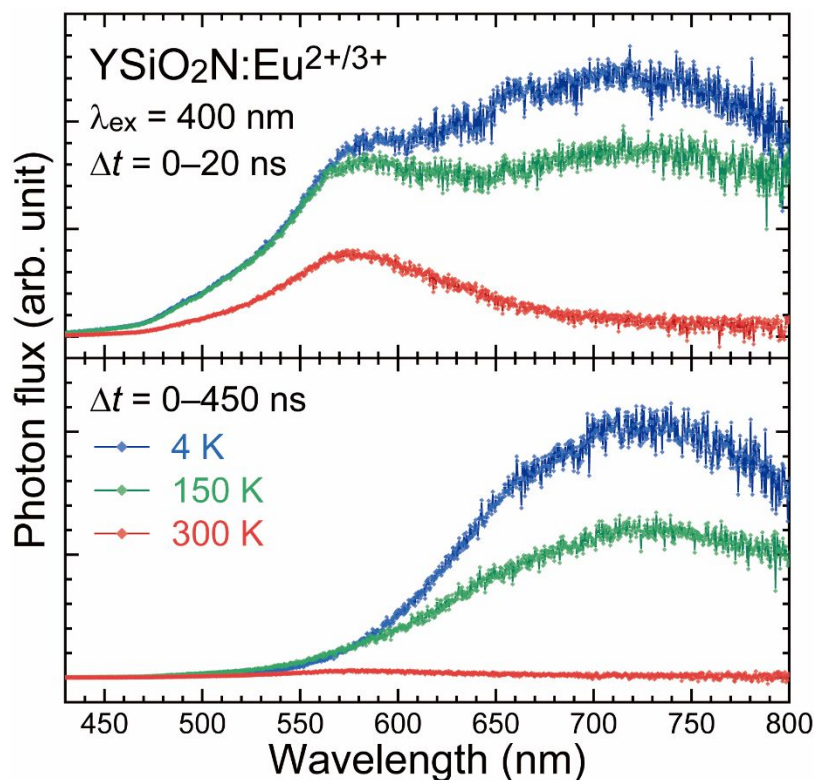
Fig. 4 Integrated time-resolved PL spectra at 4, 150, and 300 K with different integration time ranges Δt (0–20 and 0–450 ns).

In order to characterize the two broad luminescence bands in terms of the radiative decay rate, the time-resolved PL spectra of the $YSiO_2N:Eu^{2+/3+}$ sample were obtained at different temperatures (T = 4, 150, and 300 K). Fig. 3a–3c and Fig. 3d–3f show the contour plots of the time-resolved PL spectra taken with the streak camera in the different time ranges of 0–450 and 0–20 ns, respectively. The projections of each time-resolved PL spectrum are plotted as the integrated PL spectrum with different time ranges Δt (0–450 and 0–20 ns) in Fig. 4. In the range of 0–450 ns, the deep-red luminescence related to the ETE states is observed with lifetimes of a few hundreds of nanoseconds. The PL intensity of the ETE band severely decreases with

17

temperatures, as shown in the integrated PL spectra with $\Delta t = 0$–450 ns. At 300 K, the ETE luminescence is almost quenched, and only a luminescence band with a fast decay is observed. Fig. 3d–3f and 4 show that this luminescence band has a very short lifetime on the order of a few nanoseconds. The band shape and lifetime of this luminescence seem not to be affected by temperature. The time-resolved PL spectrum of the non-doped $YSiO_2N$ sample with the same measurement condition at 4 and 300 K is provided in Fig. S4 (ESI†), showing the PL band with the same decay time, spectral shape, and thermal stability. Therefore, it is suggested that the luminescence band independent of doped lanthanoid ions in the range of 480–800 nm with a ns-order lifetime is due to intrinsic defects in the $YSiO_2N$ host.

3.3 Thermal quenching behavior of Eu^{2+}-trapped exciton and defects related luminescence
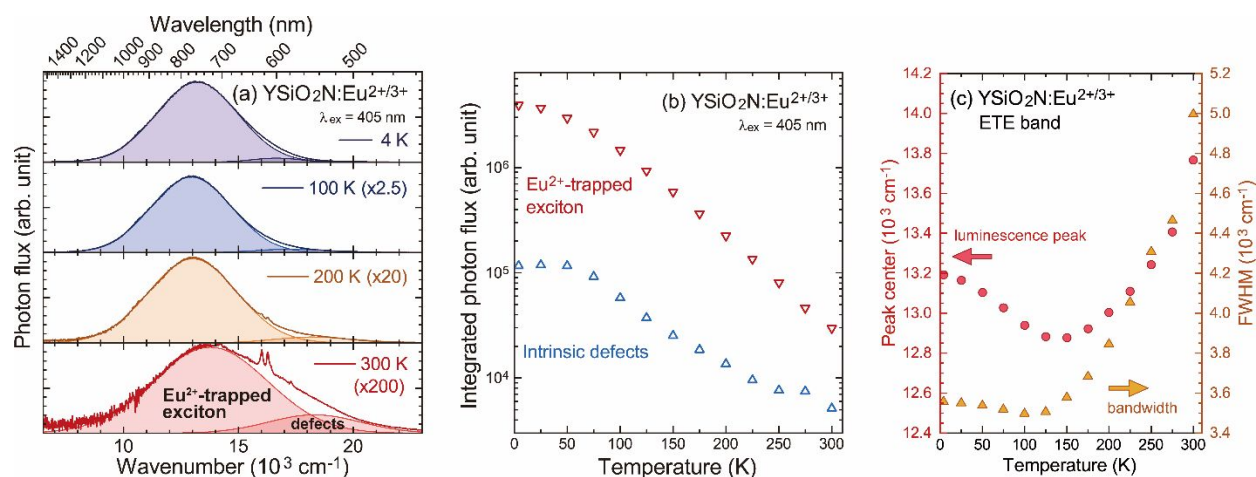
Fig. 5 (a) PL spectra ($T = 4$, 100, 150, and 300 K) with two Gaussian profiles related to the Eu^{2+}-trapped exciton state and intrinsic defects. (b) Temperature dependence of the integrated PL intensities for the Eu^{2+}-related exciton and intrinsic defects. (c) Temperature dependence of the peak center and FWHM for the Gaussian profiles of the ETE band.

The broad luminescence bands observed in the $YSiO_2N:Eu^{2+/3+}$ sample are mainly composed of two luminescence centers; Eu^{2+}-trapped exciton (ETE) state and intrinsic defects. The thermal quenching behaviors of two luminescence centers were characterized by the analyses of the temperature dependence of the PL spectra and luminescence lifetimes. Because two luminescence bands severely overlap in the PL spectra at low temperatures ($T = 4–300$ K), we first deconvoluted the PL band at each temperature into two Gaussian profiles to discuss each temperature dependence separately. As shown in Fig. 5a, the spectra were well fitted by two Gaussian profiles, the ETE and defects luminescence bands. All the obtained Gaussian profiles at the temperatures of 4–300 K are plotted in Fig. S5 (ESI†). Fig. 5b displays the temperature dependence of the integrated PL intensity for these two luminescence bands. Despite the very short lifetime, the PL intensity of intrinsic defects is much weaker than that of the ETE luminescence, indicating that the number of luminescence centers related to intrinsic defects, such as $O_N^{\cdot}$, $N_O^{\prime}$, and $V_N^{\cdot\cdot\cdot}$, is much smaller than that of the ETE centers. The quenching profile of the ETE luminescence cannot be described by the typical quenching curve, possibly due to the temperature dependence of the absorption coefficient.

The temperature-dependent peak center and FWHM of the ETE luminescence band are plotted in Fig. 5c, which shows two different behavior against temperature increase; from 4 to 150 K, the luminescence wavelength gets redshifted with temperature increasing while the bandwidth is almost unchanged; over 150 K, as the temperature increases, the luminescence wavelength gets blueshifted by about 1000 cm^{-1}, and the bandwidth gets broader up to ~4300 cm^{-1}. The blueshift of the ETE luminescence band has been reported in the literature. For the ETE luminescence of the $CsCaF_3:Eu^{2+}$, $Ba_{0.3}Sr_{0.7}F_2:Eu^{2+}$, and $Sr_4Al_{14}O_{25}:Eu^{2+}$ phosphors, the blueshift of the luminescence band was caused by the emergence of a different luminescence band at shorter

wavelength side, which is explained by the thermally enhanced change of electron population through the crossover of the ETE and Eu^{2+} $4f^6 5d^1$ parabolas.[44–46] However, the Gaussian-shaped single ETE luminescence band of the $YSiO_2N:Eu^{2+/3+}$ sample shifted without any other luminescence band emerging. Although a similar blueshift and thermal broadening of the ETE luminescence band was observed in the $BaS:Eu^{2+}$ phosphor, which was reported by Smet *et al.* (λ_{em} = 938 nm at 70 K → λ_{em} = 878 nm at 300 K, the energy shift was ~730 cm^{-1}), the reason of the spectral shape changing was not discussed in detail.[25] The spectral shape of the ETE luminescence band for the $YSiO_2N:Eu^{2+/3+}$ sample can depend on the following two factors;

1. The ETE state is influenced by the temperature dependence of the bandgap. As the temperature increases, the bandgap becomes narrower because of an increase in the amplitudes of atomic vibrations. While the electron population on the vibrational levels of the potential parabolas is unchanged at quite low temperatures, the conduction band (CB) bottom and ETE state are lowered, resulting in the redshift of the ETE luminescence band with almost no change in bandwidth. A similar shift accompanied by the bandgap shift was observed in the pressure dependence of the ETE luminescence for the $LiBaF_3:Eu^{2+}$ phosphor.[47] By inducing the pressure, the bandgap became wider, and the CB bottom and ETE state shifted higher, leading to the blueshifted ETE luminescence.

2. The spectral shapes of the broad luminescence band can be affected by the electron population on the excited states that obeys the Boltzmann distribution. With the temperature increasing, the excited electrons are distributed along the potential curve to the higher vibrational levels coupled with several phonons, resulting in the blueshifted luminescence band with a broader bandwidth. This temperature dependence is also observed in the normal Eu^{2+}: 5d → 4f luminescence.[48]

At low temperatures, these two factors compete and lead to the abnormal temperature behavior of the peak wavelength and bandwidth of the ETE luminescence band for the $YSiO_2N:Eu^{2+/3+}$ sample; *i.e.*, at low temperatures below 150 K, the influence of the temperature dependence of the bandgap is dominant; on the other hand, over 150 K, the electronic transition from the higher vibrational levels causes the thermal broadening and blueshift of the ETE luminescence band.
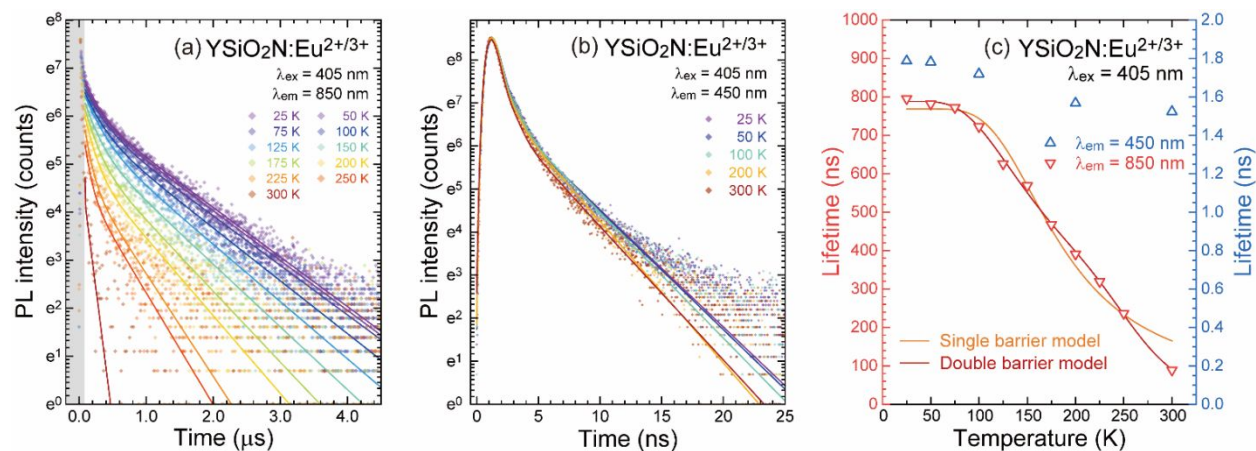
Fig. 6 (a) Luminescence decay curves at various temperatures ($T = 20–300$ K) with the monitored wavelengths of (a) $\lambda_{em} = 850$ nm and (b) $\lambda_{em} = 450$ nm. (c) Temperature dependence of the luminescence lifetimes estimated by second-order exponential functions. The solid curves represent the fitting functions with the single (orange) and double (red) quenching barrier models.

From the results of the time-resolved PL spectra and the deconvolution of PL bands, the monitoring wavelengths for the decay measurements of the luminescence related to the ETE states and intrinsic defects are determined to be 850 and 450 nm, respectively, to avoid the overlap of these bands. Fig. 6a shows the decay curves of the ETE luminescence. Each decay curve shows a deviation from the single exponential profile. Thus, all the luminescence decay curves were fitted with a second-order exponential function, described below;

$$I(t) = A_1 \exp\left(-t/\tau_1\right) + A_2 \exp\left(-t/\tau_2\right), \#(1)$$

where A_1 and A_2 are amplitudes for each decay component and τ_1 and τ_2 are the luminescence lifetime at each temperature. The initial part of the ETE luminescence decay curves below 100 ns was eliminated for the better overall fitting because the influence of excitation pulse or the defect-related luminescence is not negligible over 100 K. The fitted profiles are shown in solid lines in Fig. 6a. The average luminescence lifetime at each temperature τ_{ave} was calculated by the following equation;

$$\tau_{ave} = \frac{A_1 \tau_1^2 + A_2 \tau_2^2}{A_1 \tau_1 + A_2 \tau_2}. \#(2)$$

Fig. 6b shows the luminescence decay curves related to intrinsic defects. They were also fitted with a second-order exponential function, and their average lifetimes were estimated. For the luminescence decay curves related to intrinsic defects, the instrumental response function (IRF) was taken into account in the overall fitting.

Fig. 6c shows the temperature dependence of the lifetimes of the ETE and intrinsic defects luminescence. The decay rate of the luminescence related to intrinsic defects is mostly unchanged even at 300 K despite the significant decrease in the PL intensity, which is the same as the trend suggested from the time-resolved PL spectra (Fig. 3d–3f).

On the other hand, the ETE luminescence lifetime (770 ns at 4 K) shows a monotonous decrease over 50 K and reaches a lifetime of 89 ns at 300 K. In order to estimate the activation energy for thermal quenching, we performed the profile fitting with the typical single barrier quenching model described below;

$$\tau = \frac{1}{\Gamma_v + \Gamma_0 \exp\left(-\frac{E_a}{kT}\right)}.\#(3)$$

Here, Γ_v is the radiative transition rate, Γ_0 is the attempt rate of the non-radiative process, E_a is the activation energy of thermal quenching, k is the Boltzmann constant (= 8.617×10^{-5} eV K^{-1}), and T is temperature. The fitting function with the parameters ($\Gamma_v = 1.30 \times 10^6$ s^{-1}, $\Gamma_0 = 4.95 \times 10^7$ s^{-1}, and $E_a = 0.0605$ eV) is depicted in the solid orange curve in Fig. 6c, which largely deviates from the ETE lifetime plot. The Γ_0 for the quenching process, such as thermal ionization and thermal activation crossover, usually takes the value with the order of 10^{10}–10^{12} s^{-1}.[49] However, the estimated Γ_0 for the ETE luminescence was quite small, indicating that a simple quenching process with a single potential barrier no longer describes the thermal quenching behavior of the ETE state in the YSiO$_2$N host. In literature, the thermal quenching of the ETE luminescence is discussed by assuming the competition of two quenching processes; from the Arrhenius plot, Smet et $al.$ obtained the thermal activation energies of 14 and 190 meV for the ETE luminescence of the BaS:Eu^{2+} phosphor, which correspond to the exciton dissociation and thermal ionization, respectively;[25] Mahlik et $al.$ obtained the activation energies of 33 and 273 meV for the Ba$_{0.5}$Sr$_{0.5}$F$_2$:Eu^{2+} phosphor, related to the tunnelling from the higher vibronic levels and thermal activation crossover, respectively.[44] In order to improve the fitting results, we applied the double barrier quenching model to the profile fitting, described below;

$$\tau = \frac{1}{\Gamma_v + \Gamma_{0I} \exp\left(-\frac{E_{aI}}{kT}\right) + \Gamma_{0II} \exp\left(-\frac{E_{aII}}{kT}\right)},\#(4)$$

where the Γ_0 and E_a for the quenching processes I and II are labeled with the subscripts. The profile was well fitted with the parameters of $\Gamma_v = 1.27 \times 10^6$ s^{-1}, $\Gamma_{0I} = 1.16 \times 10^7$ s^{-1}, $\Gamma_{0II} = 6.34 \times 10^{10}$ s^{-1}, $E_{aI} = 0.0394$ eV, and $E_{aII} = 0.235$ eV. Although the Γ_{0I} value is still low, the fitting result seems

to be good. The low Γ_{0I} value can be derived from the complicated thermal quenching pathways for the ETE luminescence, such as the energy transfer to Eu^{3+} ions or intrinsic defects and a slight difference in decay rates of ETE states with the variation of incorporated sites. Nevertheless, the fitting results indicate that as least two quenching processes with the activation energies of 39.4 and 235 meV can be involved.

3.4 Mechanism of Eu^{2+}-trapped exciton luminescence in YSiO$_2$N
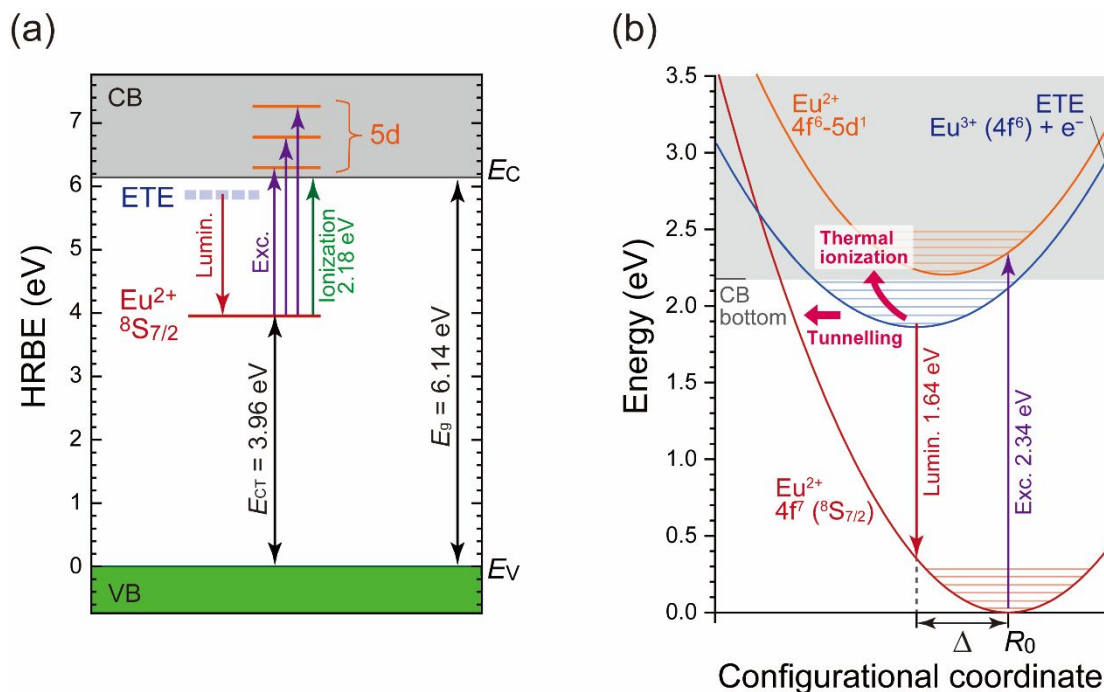
Fig. 7 (a) Constructed energy level diagram for Eu^{2+} ions in the YSiO$_2$N host. The *y*-axis is converted to the vacuum referred binding energy (VRBE). (b) Configurational coordinate diagram representing the energy level structure of the Eu^{2+} ion and Eu^{2+}-trapped exciton states.

In this section, we discuss the mechanism of the anomalous deep-red to NIR luminescence in the YSiO$_2$N:Eu$^{2+/3+}$ sample with the energy diagrams. The ETE luminescence is strongly correlated with the relative energy of the Eu^{2+}: 5d excited levels with respect to the host conduction band (CB).[26,50] Fig. 7a shows the energy level diagram of the YSiO$_2$N:Eu$^{2+/3+}$ sample, whose *y*-axis is represented in host referred binding energy (HRBE).[51–55] The bandgap energy E_g at a low temperature was obtained from the host-exciton creation energy E^{ex} by adding the exciton binding energy estimated as $0.008(E^{ex})^2$.[56,57] From the PLE spectrum of the annealed YSiO$_2$N:Eu^{3+} sample

shown in Fig. S6 (ESI†), the E^{ex} value for $YSiO_2N$ was estimated to be 5.87 eV, resulting in the

E_g of 6.14 eV. The energy difference between the VB top and Eu^{2+} 4f ground level, which

corresponds to the CT energy E_{CT} for Eu^{3+} ions, was determined to be 3.96 eV from the PLE

spectrum of the annealed $YSiO_2N:Eu^{3+}$ sample in Fig. 2d. These values lead to the ionization

energy of 2.18 eV, which is the energy gap between the ground level of $Eu^{2+}(^8S_{7/2})$ and the CB

bottom. Because the lowest 5d excited level is 2.34 eV higher than the 4f ground level, all the 5d

excited levels are located within the CB. Thus, the 5d excited states are easily deactivated because

of the strong autoionization through the CB,[25] and no 5d → 4f luminescence is observed. After the

autoionization, the ETE states of Eu^{3+} + e^- can be formed. Although the direct excitation band

related to the transition from the 4f to the ETE states in the PLE spectra was not observed, the ETE

states can be formed below the CB bottom.[44]

In order to consider the luminescence behavior after structural relaxation in the ground and

excited states, the configurational coordinate diagram for the $YSiO_2N:Eu^{2+/3+}$ is constructed and

provided in Fig. 7b. Here, the R_0 and Δ represent the equilibrium position of a Eu^{2+} ion to ligands

and the shift of ligands in the ETE state (*i.e.*, the offset of the ETE parabola). As observed in the

PLE spectra in Fig. 2c, the Eu^{2+} ground state ($4f^7$) is excited to the 5d excited states ($4f^6$-$5d^1$),

according to the Franc-Condon principle. The absence of the Eu^{2+}: 5d → 4f luminescence implies

that the Eu^{2+} $4f^6$-$5d^1$ parabola buries in the CB. The recent *ab initio* study has revealed that the

bond length between a Eu^{2+} ion and ligands in the $Eu^{2+}(4f^6$-$5d^1)$ excited states is shorter than that

in the $Eu^{2+}(4f^7)$ ground states.[58,59] In the 5d excited states, the hole generated in the inner 4f shell

attracts the ligands stronger, resulting in a short bond length of excited states and the negative

offset in the configurational coordinate diagram.[60] The parabola for the ETE state is located below

the CB bottom with the luminescence energy of 1.64 eV. For the ETE state, the electronic

configuration is described to be $Eu^{3+}(4f^6) + e^-$, indicating that an electron is weakly bound by a Eu^{3+} ion. The energy of the ETE parabola at R_0 is slightly smaller than the CB bottom by the binding energy of the exciton. This parabola has a larger negative offset Δ than the parabola for the $Eu^{2+}(4f^6\text{-}5d^1)$ configuration because the trivalent state brings about a stronger Coulomb attraction and a smaller ionic radius than the divalent states.[26] Despite the absence of any ETE absorption bands, the excited states relax down along the ETE parabola, resulting in the deep-red to NIR luminescence from the ETE states in the $YSiO_2N:Eu^{2+/3+}$ sample. The necessary condition for the ETE luminescence is that the Eu^{2+}: 5d levels are degenerated with the CB or located just below the CB bottom. As mentioned by Dorenbos, the divalent lanthanoid ion incorporated in a trivalent cation site show no 5d → 4f luminescence because the Coulomb attraction is small and the 5d level is located above the CB bottom.[26] Besides, the trivalent site can stabilize the ETE state with $Eu^{3+}(4f^6)\text{-}e^-$ configuration because of the valence state matching. Therefore, the Y^{3+} sites, which can accommodate Eu^{2+} ions, play an important role in the anomalous deep-red to NIR luminescence in the $YSiO_2N:Eu^{2+/3+}$ sample.

The thermal quenching behavior of the ETE luminescence is discussed by the configurational coordinate diagram in Fig. 7b. According to Smet,[25] the thermal quenching process of the ETE luminescence is explained by the thermal ionization of the ETE state to the CB, which is supported by the blueshifted and broadened ETE band (Fig. 5c) caused by the Boltzmann distribution on the vibrational levels. In the diagram, the energy gap between the lowest energy of the ETE state and the CB bottom, which is the ionization energy of the ETE state, is relatively small to cause the thermal quenching of the anomalous luminescence even below 300 K. The observed activation energy of 235 meV for the $YSiO_2N:Eu^{2+/3+}$ sample corresponds to the constructed energy level diagram. Also, it is a typical value, such as the activation energy for ETE

luminescence of 190 meV in BaS:Eu^{2+} and of 273 meV in $Ba_{0.5}Sr_{0.5}F_2$:Eu^{2+}. The double-barrier

quenching fitting reveals a quenching pathway with a small activation energy of 39.4 meV, which

can be related to the exciton binding energy or the thermally activated tunnelling process.[25,44] As

mentioned in the previous section, the actual energy level diagram should be more complicated

due to various defects in the $YSiO_2N$:$Eu^{2+/3+}$ sample, including intrinsic defects, Eu^{3+} ions, and

Eu^{2+} ions in different sites. These defects can act as some quenching center, resulting in the

complicated quenching behavior shown in Fig. 6c. For the identification of the thermal quenching

pathways for the ETE state in the $YSiO_2N$ host, it is necessary to investigate the luminescence

properties of the $YSiO_2N$ doped with only Eu^{2+} ions with low concentration.

4   Conclusions

Photoluminescence properties of the Eu-doped $YSiO_2N$ sample at low temperatures were investigated in detail. The X-ray absorption spectroscopy revealed that almost half Eu ions in the sample were reduced into a divalent state through the high-temperature synthesis under the inert atmosphere. The as-made sample, including Eu^{2+} ions, showed the deep-red to near-infrared luminescence at low temperatures below 300 K. This luminescence is anomalous in terms of the following points;

- The photoluminescence band took an abnormally large bandwidth (4061 cm^{-1}) and Stokes shift (5677 cm^{-1}) even at 4 K, not assigned to the typical Eu^{2+}: 5d-4f transition.

- Deep-red to near-infrared luminescence only at low temperatures was observed, which is not anticipated from the 5d-4f luminescence of other Eu^{2+}-doped (oxy)nitrides, despite not such a large N/O ratio.

- The temperature dependence of luminescence lifetime was complicated, which could not be explained by a simple quenching model.

These features indicated that the anomalous luminescence in the $YSiO_2N$:Eu sample is related to the Eu^{2+}-trapped exciton state. The vacuum referred binding energy diagram suggests that the typical Eu^{2+}: 5d $\rightarrow$ 4f luminescence is not observed because all the Eu^{2+}: 5d excited levels degenerate with the host conduction band. The configurational coordinate diagram explained the anomalous luminescence from the Eu^{2+}-trapped exciton states (Eu^{3+} + e^-) which were located just below the conduction band bottom, by taking the lattice relaxation into account. This study provides new insight into the Eu^{2+}-trapped exciton luminescence in Y sites to obtain the deep-red

to near-infrared luminescence, leading to new candidates for near-infrared applications, such as lighting, sensing, and bio-imaging devices.

Conflicts of interest

There are no conflicts of interest to declare.

Acknowledgements

References

1   K. Uheda, N. Hirosaki, Y. Yamamoto, A. Naito, T. Nakajima and H. Yamamoto, *Electrochem. Solid State Lett.*, 2006, **9**, H22–H25.

2   R.-J. Xie, N. Hirosaki, T. Suehiro, F.-F. Xu and M. Mitomo, *Chem. Mater.*, 2006, **18**, 5578–5583.

3   H. Watanabe, H. Wada, K. Seki, M. Itou and N. Kijima, *J. Electrochem. Soc.*, 2008, **155**, F31–F36.

4   P. Pust, V. Weiler, C. Hecht, A. Tücks, A. S. Wochnik, A. K. Henß, D. Wiechert, C. Scheu, P. J. Schmidt and W. Schnick, *Nat. Mater.*, 2014, **13**, 891–896.

5   S. Schmiechen, H. Schneider, P. Wagatha, C. Hecht, P. J. Schmidt and W. Schnick, *Chem. Mater.*, 2014, **26**, 2712–2719.

6   T. Matsuzawa, Y. Aoki, N. Takeuchi and Y. Murayama, *J. Electrochem. Soc.*, 1996, **143**, 2670–2673.

7   J. Ueda, T. Shinoda and S. Tanabe, *Opt. Mater. Express*, 2013, **3**, 787–793.

8   T. Kobayasi, S. Mroczkowski, J. F. Owen and L. H. Brixner, *J. Lumin.*, 1980, **21**, 247–257.

9   S. H. M. Poort, A. Meyerink and G. Blasse, *J. Phys. Chem. Solids*, 1997, **58**, 1451–1456.

10   P. Dorenbos, *J. Lumin.*, 2003, **104**, 239–260.

11   J. McKittrick and L. E. Shea-Rohwer, *J. Am. Ceram. Soc.*, 2014, **97**, 1327–1352.

12   V. Rajendran, H. Chang and R.-S. Liu, *Opt. Mater. X*, 2019, **1**, 100011.

13   J. J. Joos, D. Van der Heggen, L. I. D. J. Martin, L. Amidani, P. F. Smet, Z. Barandiarán and L. Seijo, *Nat. Commun.*, 2020, **11**, 3647.

14   Y. Wei, P. Dang, Z. Dai, G. Li and J. Lin, *Chem. Mater.*, 2021, **33**, 5496–5526.

15   W. Xie, W. Jiang, R. Zhou, J. Li, J. Ding, H. Ni, Q. Zhang, Q. Tang, J.-X. Meng and L. Lin, *Inorg. Chem.*, 2021, **60**, 2219–2227.

16   N. Yamashita, *J. Electrochem. Soc.*, 1993, **140**, 840–843.

17   I. V. Berezovskaya, V. P. Dotsenko, A. S. Voloshinovskii and S. S. Smola, *Chem. Phys. Lett.*, 2013, **585**, 11–14.

18   L. Zhou, P. A. Tanner, W. Zhou, Y. Ai, L. Ning, M. M. Wu and H. Liang, *Angew. Chem. Int. Ed Engl.*, 2017, **56**, 10357–10361.

19   J. Qiao, G. Zhou, Y. Zhou, Q. Zhang and Z. Xia, *Nat. Commun.*, 2019, **10**, 5267.

20   Q. Zhang, X. Wang, Z. Tang and Y. Wang, *Chem. Commun.*, 2020, **56**, 4644–4647.

21   Z. Tang, Q. Zhang, Y. Cao, Y. Li and Y. Wang, *Chem. Eng. J.*, 2020, **388**, 124231.

22   L. Wang, R.-J. Xie, T. Suehiro, T. Takeda and N. Hirosaki, *Chem. Rev.*, 2018, **118**, 1951–2009.

23   J. Schölch, T. Dierkes, D. Enseling, M. Ströbele, T. Jüstel and H.-J. Meyer, *Z. Anorg. Allg. Chem.*, 2015, **641**, 803–808.

24   C. Poesl and W. Schnick, *Chem. Mater.*, 2017, **29**, 3778–3784.

25   P. F. Smet, J. E. Van Haecke, F. Loncke, H. Vrielinck, F. Callens and D. Poelman, *Phys. Rev. B*, 2006, **74**, 035207.

26   P. Dorenbos, *J. Phys. Condens. Matter*, 2003, **15**, 2645–2665.

27   M. Grinberg and S. Mahlik, *Crystallogr. Rep.*, 2013, **58**, 139–143.

28   Z. Barandiarán and L. Seijo, *J. Chem. Phys.*, 2014, **141**, 234704.

29   C. MacKeen, F. Bridges, M. Kozina, A. Mehta, M. F. Reid, J.-P. R. Wells and Z. Barandiarán, *J. Phys. Chem. Lett.*, 2017, **8**, 3313–3316.

30   Y. Kitagawa, J. Ueda, M. G. Brik and S. Tanabe, *Opt. Mater.*, 2018, **83**, 111–117.

31   Y. Kitagawa, J. Ueda, K. Fujii, M. Yashima, S. Funahashi, T. Nakanishi, T. Takeda, N. Hirosaki, K. Hongo, R. Maezono and S. Tanabe, *Chem. Mater.*, 2021, **33**, 8873–8885.

32   V. Viallet, J.-F. Marucco, J. Saint, M. Herbst-Ghysel and N. Dragoe, *J. Alloys Compd.*, 2008, **461**, 346–350.

33   K. Momma and F. Izumi, *J. Appl. Crystallogr.*, 2011, **44**, 1272–1276.

34   B. Ravel and M. Newville, *J. Synchrotron Radiat.*, 2005, **12**, 537–541.

35   J. A. Sampaio, M. C. Filadelpho, A. A. Andrade, J. H. Rohling, A. N. Medina, A. C. Bento, L. M. da Silva, F. C. G. Gandra, L. A. O. Nunes and M. L. Baesso, *J. Phys. Condens. Matter*, 2010, **22**, 055601.

36   G. Z. Cao and R. Metselaar, *Chem. Mater.*, 1991, **3**, 242–252.

37   J. W. H. van Krevel, J. W. T. van Rutten, H. Mandal, H. T. Hintzen and R. Metselaar, *J. Solid State Chem.*, 2002, **165**, 19–24.

38   R.-J. Xie, M. Mitomo, K. Uheda, F.-F. Xu and Y. Akimune, *J. Am. Ceram. Soc.*, 2004, **85**, 1229–1234.

39   R.-J. Xie, N. Hirosaki, K. Sakuma, Y. Yamamoto and M. Mitomo, *Appl. Phys. Lett.*, 2004, **84**, 5404–5406.

40   R.-J. Xie, N. Hirosaki, M. Mitomo, Y. Yamamoto, T. Suehiro and K. Sakuma, *J. Phys. Chem. B*, 2004, **108**, 12027–12031.

41   R.-J. Xie, N. Hirosaki, H.-L. Li, Y. Q. Li and M. Mitomo, *J. Electrochem. Soc.*, 2007, **154**, J314–J319.

42   P. Dorenbos, *J. Lumin.*, 2000, **91**, 91–106.

43   P. Dorenbos, *J. Phys. Condens. Matter*, 2003, **15**, 575–594.

44   S. Mahlik, K. Wiśniewski, M. Grinberg and R. S. Meltzer, *J. Phys. Condens. Matter*, 2009, **21**, 245601.

45   U. Happek, M. Aycibin, A. M. Srivastava, H. Comanzol and S. Camardello, *ECS Trans.*, 2009, **25**, 39–43.

46   D. Dutczak, C. Ronda, T. Jüstel and A. Meijerink, *J. Phys. Chem. A*, 2014, **118**, 1617–1621.

47   S. Mahlik, K. Wisniewski, M. Grinberg and H. J. Seo, *J. Non-Cryst. Solids*, 2010, **356**, 1888–1892.

48   J. Ueda, S. Tanabe, K. Takahashi, T. Takeda and N. Hirosaki, *Bull. Chem. Soc. Jpn.*, 2018, **91**, 173–177.

49   P. Dorenbos, *J. Lumin.*, 2018, **197**, 62–65.

50   M. Grinberg, *Opt. Mater.*, 2013, **35**, 2006–2012.

51   P. Dorenbos, *Phys. Rev. B*, 2012, **85**, 165107.

52   P. Dorenbos, *ECS J. Solid State Sci. Technol.*, 2012, **2**, R3001–R3011.

53   P. Dorenbos, *J. Lumin.*, 2013, **135**, 93–104.

54   P. Dorenbos, *J. Lumin.*, 2013, **136**, 122–129.

55   Y. Kitagawa, J. Ueda and S. Tanabe, *Phys. Status Solidi A.*, *in press*. DOI:10.1002/pssa.202100670

56   P. Dorenbos, *Opt. Mater.*, 2017, **69**, 8–22.

57   T. Lyu and P. Dorenbos, *J. Mater. Chem. C*, 2018, **6**, 369–379.

58   Z. Barandiarán and L. Seijo, *J. Chem. Phys.*, 2003, **119**, 3785–3790.

59   J. J. Joos, P. F. Smet, L. Seijo and Z. Barandiarán, *Inorg. Chem. Front.*, 2020, **7**, 871–888.

60   W. Gryk, D. Dyl, W. Ryba-Romanowski and M. Grinberg, *J. Phys. Condens. Matter*, 2005, **17**, 5381–5395.